Transmission Torque Model and Experimental Verification of Slotted Axial Magnetic Coupler

Ao Wang

Abstract—**A novel 2-D vector magnetic potential analysis model is employed to forecast the transmission torque of a slotted axial magnetic coupler. A 2-D Cartesian coordinate system is established on the conductor sheet, and the slotted axial magnetic coupler is subsequently divided into five distinct regions. Utilizing Ohm's law, the equivalent permeability and conductivity of the slotted conductor sheet region are calculated. Considering the permanent magnet (PM) region as the source of a time-varying magnetic field, the multi-layer boundary value problem is solved, leading to the computation of the output torque. To investigate the variation in output torque of the slotted axial magnetic coupler with respect to the slip rate under various air gap thicknesses, an experimental platform is constructed. A comparative analysis is performed between the experimental results and the predictions of the theoretical model, revealing that the deviation rate remains below 5% within a slip rate range of 0 to 0.3, indicative of strong agreement. This finding serves as a solid theoretical foundation for the optimal design and optimization of the slotted axial magnetic coupler.**

Index Terms—**vector magnetic potential, slotted axial magnetic coupler, conductor sheet, permanent magnet (PM).**

I. Introduction

MAGNETIC coupler is a novel torque transmission device that harnesses the rotation between a permanent magnet (PM) and a conductor to generate an electromagnetic force. This magnetic coupling enables torque transfer without any physical contact between the drive and load ends, thereby offering advantages over traditional couplings, including soft starting capabilities, overload protection, and frictionless operation. Its widespread adoption in industrial sectors, notably transmission and braking systems, underscores its significance and potential [1-4].

In general, magnetic couplers feature a grooveless structure. To enhance the magnetic field strength in the air gap of the magnetic coupler, a topology with slots in the conductor disk is proposed. Compared to traditional unslotted structures, magnetic couplers with slotted conductor disks exhibit a higher torque density [5]. The analysis and design of magnetic couplers can be undertaken through numerical and analytical methods. The numerical method predominantly involves the finite element method (FEM) [6-8], which efficiently addresses the eddy current issue in moving conductors and provides accurate transmission torque results. However, FEM is plagued by lengthy calculation times, limited flexibility, and high hardware requirements, thereby restricting its universal applicability. Conversely, analytical methods generally demand fewer computing resources and time. Among the existing analytical methods, the layer model approach is widely employed for magnetic couplers without a slot structure [9-11]. Another analytical technique is the equivalent magnetic circuit method [12-14], which presupposes knowledge of the magnetic flux path but may introduce substantial calculation errors for thick air gaps.

Currently, the conformal transformation method and subdomain model method are primarily employed to determine the magnetic field intensity in slotted structures [15-18]. Nevertheless, the conformal transformation method is not suitable for magnetic couplers owing to their intricate relative permeability profiles. Regarding the subdomain model method, the influence of eddy currents on the magnetic field is generally overlooked, resulting in substantial inaccuracies when studying slotted magnetic couplers [19-23].

This paper centers on the slotted axial magnetic coupler as the research subject. It utilizes Ohm's law to compute the equivalent permeability and conductivity of the conductor sheet region featuring a slot structure. By considering the PM region as the time-varying magnetic field source, it solves the multilayer boundary value problem and ultimately derives the output torque. This methodology not only circumvents the aforementioned challenges but also boasts a relatively straightforward calculation process. To validate the theoretical analysis model, an experimental test platform has been constructed.

II. Theory

A. 3-D Structure Model

Fig. 1 shows the 3-D configuration of the slotted magnetic coupler, which comprises two distinct parts: a conductor rotor and a PM rotor. The conductor rotor is made up of a conductor sheet featuring equally spaced slots running along its circumference, and a conductor back iron with evenly distributed protrusions. The PM rotor, on the other hand, incorporates a PM with a uniform alternating pattern of N and S poles, accompanied by a PM back iron.

B. Basic Equation

The basic formula of induced current and magnetization [1]

$$\nabla^2 \mathbf{A} = \mu\sigma \frac{\partial \mathbf{A}}{\partial t} - \mu_0 \nabla \times \mathbf{M} \tag{1}$$

Since

$$\frac{\partial \mathbf{A}}{\partial t} = \frac{\partial \mathbf{A}}{\partial t} \cdot \frac{\partial t}{\partial x} \cdot \frac{\partial x}{\partial t} = s\omega_1 \tau_p / \pi \cdot \frac{\partial \mathbf{A}}{\partial x} \tag{2}$$

Manuscript received April 29, 2024; revised August 5, 2024.

Ao Wang is a doctoral candidate in the School of Mechanical Engineering at Jiangsu University, Zhenjiang Jiangsu, 212013, China. (corresponding author to provide phone: 15551786981; email: wangao20220424@163.com)

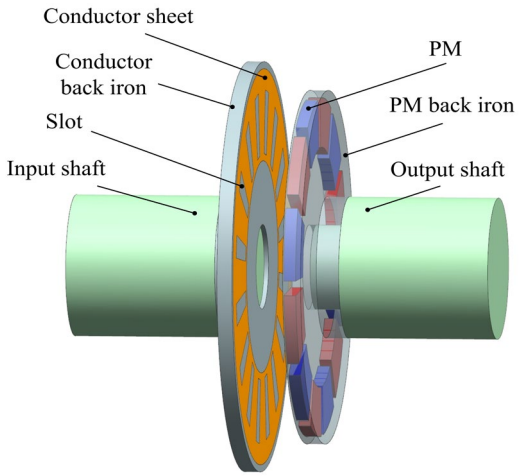

Fig.1. 3-D structure of slotted axial magnetic coupler.

where ω_1 is the actual electrical angle of the conductor layer, unit: rad/s, s is the slip rate.

$$s = \frac{n_1 - n_2}{n_1} \tag{3}$$

$$\omega_1 = \frac{2\pi n_1 p}{60} \tag{4}$$

Substitute formula (2) into (1)

$$\nabla^2 \mathbf{A} = \mu\sigma s\omega_1 \tau_p / \pi \cdot \frac{\partial \mathbf{A}}{\partial x} - \mu_0 \nabla \times \mathbf{M} \tag{5}$$

C. Regional Equation

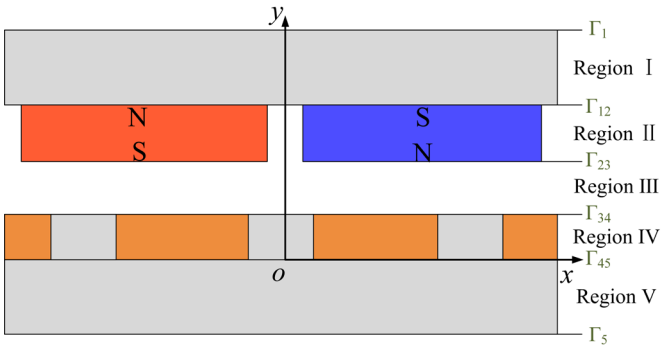

Fig. 2. 2-D model for a slotted axial magnetic coupler. (Region I: PM back iron, Region II: PM array, Region III: air gap, Region IV: conductor sheet, and Region V: conductor back iron).

Region I is the layer of the PM back iron, the back iron and the PM are relatively static and the back iron does not have magnetization, so $\mathbf{J} = 0$, $\mathbf{M} = 0$. Substitute this formula into (5) to get:

$$\nabla^2 \mathbf{A}^{\mathrm{I}} = 0 \tag{6}$$

Region II is the PM layer, there is no induced current but magnetization, so $\mathbf{J} = 0$. Substitute this formula into (5) to get:

$$\nabla^2 \mathbf{A}^{\mathrm{II}} = -\mu_0 \nabla \times \mathbf{M} \tag{7}$$

Region III is the air gap layer, there is no induced current and no magnetization, so $\mathbf{J} = 0$, $\mathbf{M} = 0$. Substitute this formula into (5) to get:

$$\nabla^2 \mathbf{A}^{\mathrm{III}} = 0 \tag{8}$$

Region IV is the conductor layer, there is induced current but no magnetization, so $\mathbf{M} = 0$. Substitute this formula into (5) to get:

$$\nabla^2 \mathbf{A}^{\mathrm{IV}} = \mu_c \sigma_c s\omega_1 \tau_p / \pi \cdot \frac{\partial \mathbf{A}}{\partial x} \tag{9}$$

where, μ_c, σ_c are the equivalent permeability and conductivity of the conductor layer, respectively. Since the conductor layer is composed of copper and iron, Ohm's law can be applied to calculate the equivalent permeability and conductivity of the conductor layer [1]

$$\begin{cases} \dfrac{\tau_q}{\mu_{cx} t_c} = \dfrac{\tau_q - \tau_i}{\mu_d t_c} + \dfrac{\tau_i}{\mu_i t_c} \\ \dfrac{1}{t_c / \mu_{cy} \tau_q} = \dfrac{1}{t_c / \mu_d (\tau_q - \tau_i)} + \dfrac{1}{t_c / \mu_i \tau_i} \\ \dfrac{1}{\omega_c / \mu_{cz} \tau_q} = \dfrac{1}{\omega_c / \mu_d (\tau_q - \tau_i)} + \dfrac{1}{\omega_c / \mu_i \tau_i} \end{cases} \tag{10}$$

$$\begin{cases} \dfrac{\tau_q}{\sigma_{cx} t_c} = \dfrac{\tau_q - \tau_i}{\sigma_d t_c} + \dfrac{\tau_i}{\sigma_i t_c} \\ \dfrac{1}{t_c / \sigma_{cy} \tau_q} = \dfrac{1}{t_c / \sigma_d (\tau_q - \tau_i)} + \dfrac{1}{t_c / \sigma_i \tau_i} \\ \dfrac{1}{\omega_c / \sigma_{cz} \tau_q} = \dfrac{1}{\omega_c / \sigma_d (\tau_q - \tau_i)} + \dfrac{1}{\omega_c / \sigma_i \tau_i} \end{cases} \tag{11}$$

where, μ_d, σ_d respectively, are the relative permeability and electrical conductivity of copper, μ_i, σ_i are the relative permeability and electrical conductivity of iron, μ_{cx}, μ_{cy} and are the relative permeability of the conductor layer in the x, y and z axis directions, σ_{cx}, σ_{cy} and σ_{cz} are the relative conductivity of the conductor layer in the x, y and z axis directions, simplified equation (10), (11)

$$\begin{cases} \mu_{cx} = \dfrac{\mu_d \mu_i}{\mu_i + (\mu_d - \mu_i)\tau_i / \tau_q} \\ \mu_{cy} = \mu_{cz} = \mu_d + (\mu_i - \mu_d)\tau_i / \tau_q \end{cases} \tag{12}$$

$$\begin{cases} \sigma_{cx} = \dfrac{\sigma_d \sigma_i}{\sigma_i + (\sigma_d - \sigma_i)\tau_i / \tau_q} \\ \sigma_{cy} = \sigma_{cz} = \sigma_d + (\sigma_i - \sigma_d)\tau_i / \tau_q \end{cases} \tag{13}$$

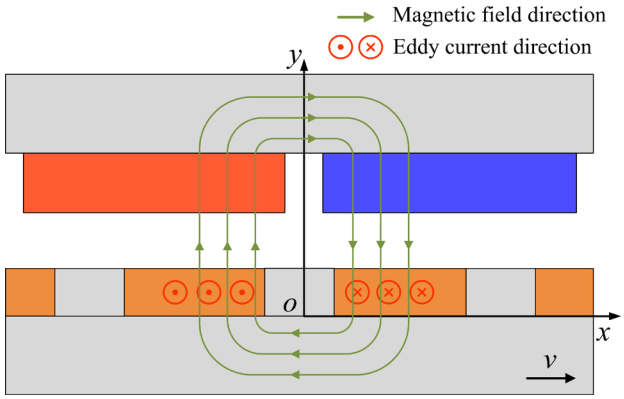

Fig. 3. 2-D magnetic circuit analytical model of slotted axial magnetic coupler.

It can be seen from Fig. 3 that the magnetic field direction

of the conductor layer is mainly along the axial direction, that is, the y axis direction, and the induced current direction is perpendicular to the xoy plane, that is, the z axis direction. Therefore, equation (9) can be simplified as

$$\nabla^2 \mathbf{A}^{\mathrm{IV}} = \mu_{\mathrm{cy}} \sigma_{cz} s\omega_1 \tau_p / \pi \cdot \frac{\partial \mathbf{A}}{\partial x} \tag{14}$$

Region V is the conductive yoke layer, with induced current but no magnetization intensity, so $\mathbf{M} = 0$. Substitute this formula into (5) to get:

$$\nabla^2 \mathbf{A}^{\mathrm{V}} = \mu_i \sigma_i s\omega_1 \tau_p / \pi \cdot \frac{\partial \mathbf{A}}{\partial x} \tag{15}$$

In a 3-D rectangular coordinate system, it can be expanded as follows

$$\nabla^2 \mathbf{A} = \frac{\partial^2 \mathbf{A}}{\partial x^2} + \frac{\partial^2 \mathbf{A}}{\partial y^2} + \frac{\partial^2 \mathbf{A}}{\partial z^2} \tag{16}$$

Since the direction of the vector magnetic potential **A** is the same as that of the current density **J** and both are in the z axis direction, using the time-harmonic field analysis method, the functional analytic formula of the vector magnetic potential **A** is as follows [24]

$$\mathbf{A}(x,y,t) = \sum_{n=1,3,5\ldots} \mathrm{Re}[\dot{A}_{zn}(x,y) e^{jnsw_1 t}] \mathbf{i}_z \tag{17}$$

where

$$\dot{A}_{zn}(x,y) = \dot{A}_{zn}(y) e^{-j\alpha_n x} \tag{18}$$

where

$$\alpha_n = \frac{n\pi}{\tau_p} \tag{19}$$

If the nth harmonic component of the field quantity has $\partial / \partial x = -j\alpha_n$ [1], it can be obtained by equations (16) and (18)

$$\frac{\partial^2 \dot{A}_{zn}}{\partial x^2} + \frac{\partial^2 \dot{A}_{zn}}{\partial y^2} + \frac{\partial^2 \dot{A}_{zn}}{\partial z^2} = \left(-\alpha_n^2 \dot{A}_{zn} + \frac{\partial^2 \dot{A}_{zn}}{\partial y^2} \right) e^{-j\alpha_n x} \tag{20}$$

Similarly, the functional analytic expression of magnetization

$$\mathbf{M}(x,t) = \sum_{n=1,3,5\ldots} \mathrm{Re}[\dot{M}_n(x) e^{jnsw_1 t}] \mathbf{i}_{\mathrm{y}} \tag{21}$$

$$\begin{aligned} \dot{M}_n(x) &= M'_n e^{-j\alpha_n x} \\ &= \frac{4B_r}{\mu_0 n\pi} \sin\left(\frac{n\pi\tau_m}{2\tau_p} \right) e^{-j\alpha_n x} \end{aligned} \tag{22}$$

where B_r is the actual residual magnetic induction intensity of the PM

$$\nabla \times \mathbf{M} = \begin{bmatrix} \mathbf{i}_x & \mathbf{i}_y & \mathbf{i}_z \\ \frac{\partial}{\partial x} & \frac{\partial}{\partial y} & \frac{\partial}{\partial z} \\ 0 & M & 0 \end{bmatrix} = \frac{\partial M}{\partial x} \mathbf{i}_z - \frac{\partial M}{\partial z} \mathbf{i}_x \tag{23}$$

For the nth harmonic component of the field quantity, it can be obtained by equations (22) and (23)

$$\frac{\partial \dot{M}_n}{\partial x} = -j\alpha_n \dot{M}_n e^{-j\alpha_n x} \tag{24}$$

Therefore, the equations (6), (7), (8), (14) and (15) are rewritten into the scalar form of the nth harmonic field equation

$$\frac{\partial^2 \dot{A}^{\mathrm{I}}_{\mathrm{zn}}}{\partial y^2} - \alpha_n^2 \dot{A}^{\mathrm{I}}_{\mathrm{zn}} = 0 \tag{25}$$

$$\frac{\partial^2 \dot{A}^{\mathrm{II}}_{\mathrm{zn}}}{\partial y^2} - \alpha_n^2 \dot{A}^{\mathrm{II}}_{\mathrm{zn}} = j\mu_0 \alpha_n \dot{M}_n \tag{26}$$

$$\frac{\partial^2 \dot{A}^{\mathrm{III}}_{\mathrm{zn}}}{\partial y^2} - \alpha_n^2 \dot{A}^{\mathrm{III}}_{\mathrm{zn}} = 0 \tag{27}$$

$$\frac{\partial^2 \dot{A}^{\mathrm{IV}}_{\mathrm{zn}}}{\partial y^2} - \left(\alpha_n^2 - j\mu_{cy} \sigma_{cz} ns\omega_1 \right) \dot{A}^{\mathrm{IV}}_{\mathrm{zn}} = 0 \tag{28}$$

$$\frac{\partial^2 \dot{A}^{\mathrm{V}}_{\mathrm{zn}}}{\partial y^2} - \left(\alpha_n^2 - j\mu_i \sigma_i ns\omega_1 \right) \dot{A}^{\mathrm{V}}_{\mathrm{zn}} = 0 \tag{29}$$

General solution for each region

$$\dot{A}^{\mathrm{I}}_{\mathrm{zn}} = \left(C^{\mathrm{I}}_n e^{\alpha_n y} + D^{\mathrm{I}}_n e^{-\alpha_n y} \right) e^{-j\alpha_n x} \tag{30}$$

$$\dot{A}^{\mathrm{II}}_{\mathrm{zn}} = \left(C^{\mathrm{II}}_n e^{\alpha_n y} + D^{\mathrm{II}}_n e^{-\alpha_n y} \right) e^{-j\alpha_n x} - j\mu_0 \dot{M}_n / \alpha_n \tag{31}$$

$$\dot{A}^{\mathrm{III}}_{\mathrm{zn}} = \left(C^{\mathrm{III}}_n e^{\alpha_n y} + D^{\mathrm{III}}_n e^{-\alpha_n y} \right) e^{-j\alpha_n x} \tag{32}$$

$$\dot{A}^{\mathrm{IV}}_{\mathrm{zn}} = \left(C^{\mathrm{IV}}_n e^{\beta_{cn} y} + D^{\mathrm{IV}}_n e^{-\beta_{cn} y} \right) e^{-j\alpha_n x} \tag{33}$$

$$\dot{A}^{\mathrm{V}}_{\mathrm{zn}} = \left(C^{\mathrm{V}}_n e^{\beta_{in} y} + D^{\mathrm{V}}_n e^{-\beta_{in} y} \right) e^{-j\alpha_n x} \tag{34}$$

where

$$\beta_{cn} = \sqrt{\alpha_n^2 - j\mu_{cy} \sigma_{cz} ns\omega_1} \tag{35}$$

$$\beta_{in} = \sqrt{\alpha_n^2 - j\mu_i \sigma_i ns\omega_1} \tag{36}$$

D. Boundary Equation

Due to the common boundary between adjacent layer regions, according to Gauss's theorem and Ampère's circuital law, the normal component of magnetic flux density in two adjacent media is equal, and the tangential component of magnetic field intensity in adjacent media is also equal. The relation between the magnetic flux density and magnetic field intensity at the boundary surface of adjacent layers is

$$B_{n1} = B_{n2} \tag{37}$$

$$H_{\tau 1} = H_{\tau 2} \tag{38}$$

where

$$B_{n1} = \frac{\partial A_1}{\partial x} \tag{39}$$

$$B_{n2} = \frac{\partial A_2}{\partial x} \tag{40}$$

$$H_{\tau 1} = \frac{1}{\mu_1} \frac{\partial A_1}{\partial y} \tag{41}$$

$$H_{\tau 2} = \frac{1}{\mu_2} \frac{\partial A_2}{\partial y} \tag{42}$$

where, B_{n1} and B_{n2} are the normal components of magnetic density of two adjacent media respectively; $H_{\tau 1}$ and $H_{\tau 2}$ are tangential components of the magnetic field intensity of

adjacent media; A_1 and A_2 are the scalar magnetic potential of two adjacent media; μ_1 and μ_2 are tangential equivalent permeability of adjacent media.

According to equations (30)-(34) and Fig. 2, it can be clearly seen that the normal direction corresponds to the direction where the y-axis is located, and the tangential direction corresponds to the direction where the x-axis is located. Therefore, the boundary conditions for the model of adjacent layers can be derived

$$\frac{\partial \dot{A}_{zn}^{\mathrm{I}}}{\partial x}=0 \quad \Gamma_1 \tag{43}$$

$$\begin{cases} \dfrac{1}{\mu_{mx}}\dfrac{\partial \dot{A}_{zn}^{\mathrm{II}}}{\partial y}=\dfrac{1}{\mu_i}\dfrac{\partial \dot{A}_{zn}^{\mathrm{I}}}{\partial y} \\ \dfrac{\partial \dot{A}_{zn}^{\mathrm{II}}}{\partial x}=\dfrac{\partial \dot{A}_{zn}^{\mathrm{I}}}{\partial x} \end{cases} \quad \Gamma_{12} \tag{44}$$

where, μ_{px} is the equivalent permeability of the PM layer in the x-axis direction. The calculation method is the same as the equivalent permeability of the conductor layer, then the equivalent permeability of the PM layer in the x-axis direction is

$$\frac{\tau_p}{\mu_{mx}t_m}=\frac{\tau_m}{\mu_m t_m}+\frac{\tau_p-\tau_m}{\mu_0 t_m} \tag{45}$$

Simplify equation (45)

$$\mu_{mx}=\frac{\mu_m\mu_0}{\mu_0\tau_m/\tau_p+\mu_m\left(1-\tau_m/\tau_p\right)} \tag{46}$$

$$\begin{cases} \dfrac{1}{\mu_0}\dfrac{\partial \dot{A}_{zn}^{\mathrm{III}}}{\partial y}=\dfrac{1}{\mu_{mx}}\dfrac{\partial \dot{A}_{zn}^{\mathrm{II}}}{\partial y} \\ \dfrac{\partial \dot{A}_{zn}^{\mathrm{III}}}{\partial x}=\dfrac{\partial \dot{A}_{zn}^{\mathrm{II}}}{\partial x} \end{cases} \quad \Gamma_{23} \tag{47}$$

$$\begin{cases} \dfrac{1}{\mu_{cx}}\dfrac{\partial \dot{A}_{zn}^{\mathrm{IV}}}{\partial y}=\dfrac{1}{\mu_0}\dfrac{\partial \dot{A}_{zn}^{\mathrm{III}}}{\partial y} \\ \dfrac{\partial \dot{A}_{zn}^{\mathrm{IV}}}{\partial x}=\dfrac{\partial \dot{A}_{zn}^{\mathrm{III}}}{\partial x} \end{cases} \quad \Gamma_{34} \tag{48}$$

$$\begin{cases} \dfrac{1}{\mu_i}\dfrac{\partial \dot{A}_{zn}^{\mathrm{V}}}{\partial y}=\dfrac{1}{\mu_{cx}}\dfrac{\partial \dot{A}_{zn}^{\mathrm{IV}}}{\partial y} \\ \dfrac{\partial \dot{A}_{zn}^{\mathrm{V}}}{\partial x}=\dfrac{\partial \dot{A}_{zn}^{\mathrm{IV}}}{\partial x} \end{cases} \quad \Gamma_{45} \tag{49}$$

$$\frac{\partial \dot{A}_{zn}^{\mathrm{V}}}{\partial x}=0 \quad \Gamma_5 \tag{50}$$

E. Electromagnetic Torque Solution

According to [1] electromagnetic force

$$F_{2D}=\pi p\sigma s\omega_1\sum_{n=1,3,5\ldots}\left(n^2\int_{y_5}^{y_{34}}\left|\dot{A}_{zn}(y)\right|^2 dy\right) \tag{51}$$

$$F_{3D}=k_s\omega_m F_{2D} \tag{52}$$

where

$$\omega_m=r_{m2}-r_{m1} \tag{53}$$

$$k_s=1-\frac{\tanh\left[\pi\omega_m/(2\tau_p)\right]}{\left[\pi\omega_m/(2\tau_p)\right]\left\{1+\tanh\left[\pi\omega_m/(2\tau_p)\right]\tanh\left[\pi(\omega_c-\omega_m)/(2\tau_p)\right]\right\}} \tag{54}$$

$$T=\left|r\times F_{3D}\right| \tag{55}$$

III. Experiment Verification For Proposed Model

A. Parameter Setting

To verify the accuracy of the model, the structural parameters and material properties of the slotted axial magnetic coupler were set. The experimental results for the verification of the model's accuracy are presented in Table I. Fig. 4 depicts the diagrams of the structural parameters of the slotted axial magnetic coupler, where Fig. 4(a) represents the radial cross-section diagram, Fig. 4(b) is the 2-D structure diagram of the PM rotor, and Fig. 4(c) shows the 2-D structure diagram of the conductor rotor. As can be seen from the figures, PMs are evenly distributed along the circumference, and the magnetic fields of adjacent PMs are opposite. Fan-shaped slots are evenly distributed along the circumference as well. Overall, the design of the slotted axial magnetic coupler features evenly distributed PMs and fan-shaped slots, which are crucial for its performance.

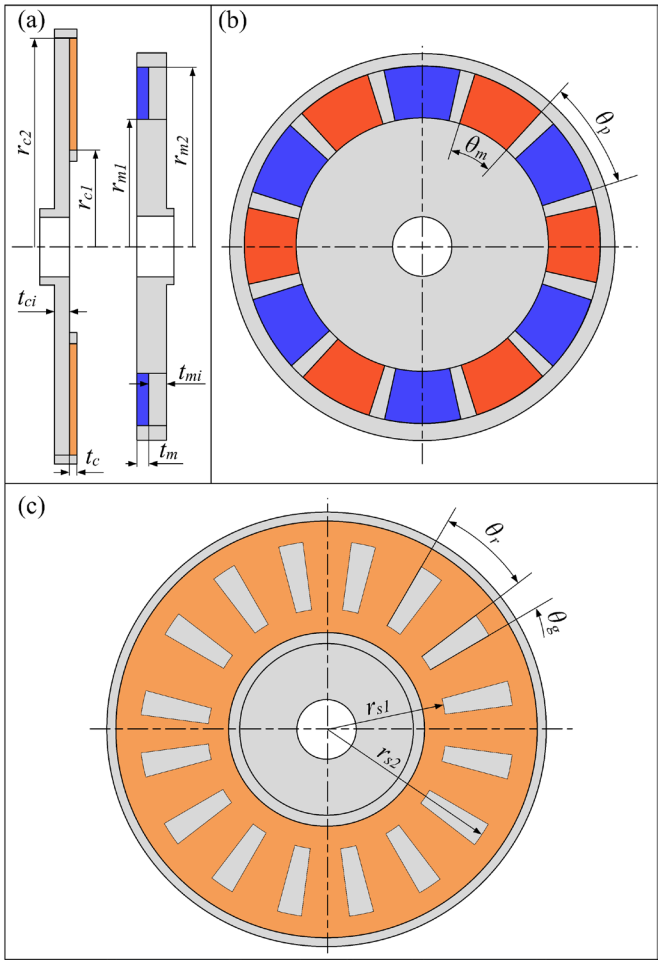

Fig. 4. Geometrical structure of slotted axial magnetic coupler. (a) Radial cross section, (b) 2-D structure of PM rotor, and (c) 2-D structure of conductor rotor.

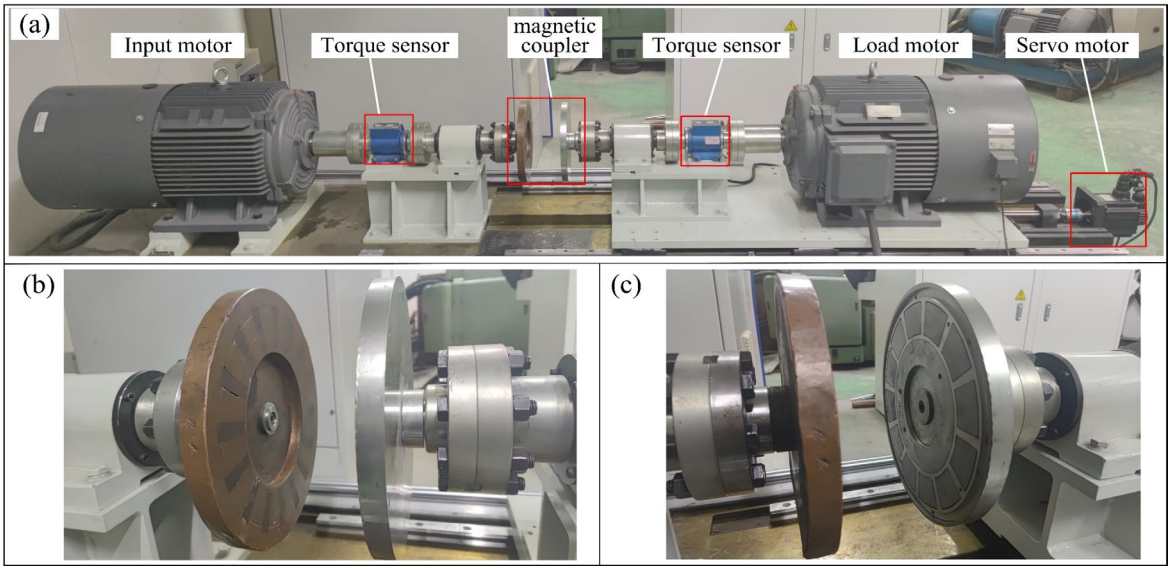

Fig. 5. Experimental platform of the testing system. (a) Experimental platform, (b) Structure of conductor rotor, and (c) Structure of PM rotor.

B. *Experimental Verification*

Fig. 5 shows the experimental setup of the magnetic coupler, which includes an input motor, a torque sensor, a slotted axial magnetic coupler, a load motor, and a servo motor. The input speed is set at 1200 rpm, with the torque sensor measuring the output torque. The air gap thickness is adjusted to 4 mm, 6 mm, and 8 mm, respectively, by controlling the servo motor. Following this, the load motor is employed to vary the output speed, enabling the conduction of magnetic drive experiments under different slip conditions.

TABLE I
SPECIFICATIONS OF SLOTTED AXIAL MAGNETIC COUPLER

Parameter	Value
Number of PM pole pairs, p	6
Air gap length, g	4–12 mm
Inner radius of the PMs, r_{m1}	85 mm
Outer radius of the PMs, r_{m2}	125 mm
Thickness of the PMs, t_m	8 mm
Inside radius of the CS, r_{c1}	75 mm
Outside radius of the CS, r_{c2}	135 mm
Thickness of the CS, t_c	5 mm
Thickness of the PM back iron, t_{mi}	12 mm
Thickness of the CS back iron, t_{ci}	10 mm
Inner radius of the slots	80 mm
Number of slots	16
Angle of pole pitch, θ_p	30°
Angle of pole-arc, θ_m	25°
Angle of slot pitch, θ_r	22.5°
Angle of slot , θ_g	7.5°
Permeability of vacuum, μ_0	$4\pi\times10^{-7}$ H/m
Relative permeability of PMs, μ_m	1.099
Relative permeability of back iron, μ_i	2000
Coercive force of the PMs, H_p	−868 kA/m
Conductivity of the copper, σ_d	5.7×10^7 S/m
Outer radius of the slots	130 mm

Fig. 6, 7, and 8 show the comparison of theoretical and experimental torque at different slip ratios under different gap thicknesses. The formula of the deviation ratio between the theoretical torque and experimental torque is as follows:

$$D=\frac{|T_e-T|}{T_e}\times100\% \tag{56}$$

where T represents theoretical torque, T_e represents experimental torque, and D represents deviation ratio.

In Fig. 6, 7, and 8, the output torque gradually increases as the slip ratio varies from 0 to 0.12, peaking at a slip ratio of 0.12. As the air gap thickness increases, the maximum value of the output torque decreases. Subsequently, the output torque gradually decreases when the slip ratio ranges from 0.12 to 0.5. Within a slip ratio of 0 to 0.3, the experimental torque exhibits good agreement with the theoretical torque, with a maximum deviation ratio of less than 5%. However, as the slip ratio exceeds 0.3, the deviation between the theoretical and experimental torques gradually increases, and the deviation ratios surpass 10% when the slip ratio reaches 0.48. This discrepancy may be attributed to the enhanced slip ratio and disturbances within the air gap magnetic field between the PM rotor and the conductor rotor

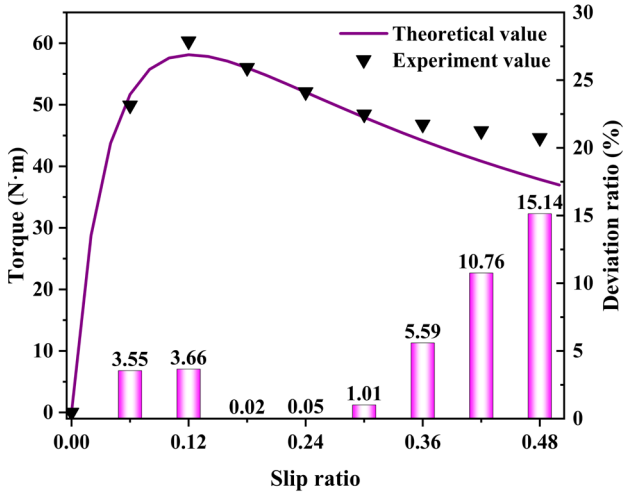

Fig. 6. Comparison of theoretical and experiment torque at different slip ratios (g=4 mm).

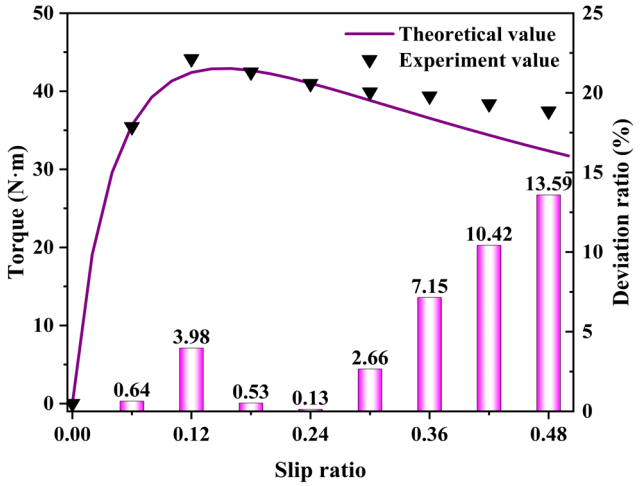

Fig. 7. Comparison of theoretical and experiment torque at different slip ratios (g=6 mm).

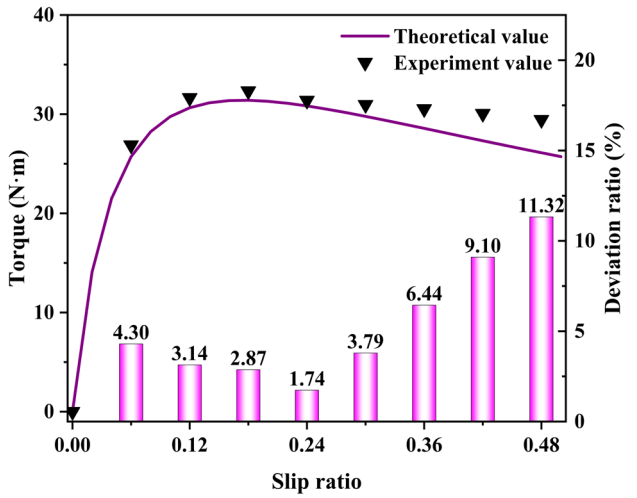

Fig. 8. Comparison of theoretical and experiment torque at different slip ratios (g=8 mm).

Fig. 9 compares the theoretical and experimental mechanical characteristic curves of the slotted axial magnetic coupler with an air gap thickness of 4 mm. When the output speed varies within the range of 840 to 1156 rpm, the theoretical values show a high degree of consistency with the experimental values. However, below 840 rpm, a notable discrepancy emerges between the theoretical and experimental values, and this gap widens as the output speed further decreases. Specifically, at an output speed of 1156 rpm, the output torque attains its maximum value of 60.3 N·m, whereas at 840 rpm, the output torque is 48.4 N·m. Consequently, within the output torque range of 48.4 to 60.3 N·m, the theoretical model effectively predicts the experimental outcomes.

Fig. 10 compares the theoretical and experimental mechanical characteristic curves of the slotted axial magnetic coupler with an air gap thickness of 6 mm. When the output speed varies within the range of 840 to 1156 rpm, the theoretical and experimental values exhibit a high degree of consistency. However, when the output speed falls below 840 rpm, a significant discrepancy arises between the theoretical and experimental values, and this discrepancy widens as the output speed further decreases. Specifically, at an output speed of 1156 rpm, the output torque achieves its maximum value of 44.2 N·m, while at 840 rpm, the output torque is 39.9 N·m. Consequently, the theoretical model is able to accurately predict the experimental results within the output torque range of 39.9 to 44.2 N·m.

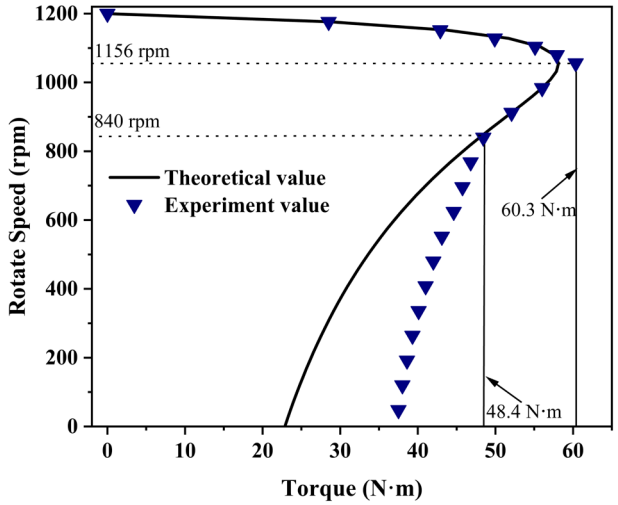

Fig. 9. Comparison of theoretical and experiment mechanical characteristic curves (g=4 mm).

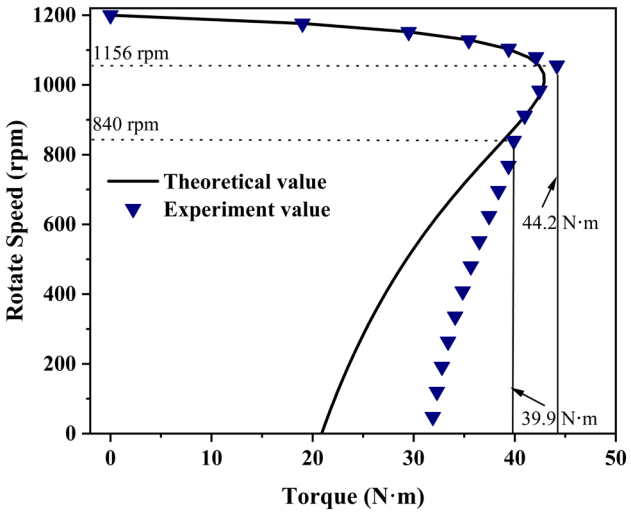

Fig. 10. Comparison of theoretical and experiment mechanical characteristic curves (g=6 mm).

Fig. 11 presents a comparison of the theoretical and experimental mechanical characteristic curves for the slotted axial magnetic coupler with an air gap thickness of 8 mm. When the output speed falls within the range of 912 to 984 rpm, the theoretical and experimental values show a high degree of consistency. However, when the output speed dips below 912 rpm, a notable discrepancy emerges between the theoretical and experimental values, and this discrepancy widens as the output speed further decreases. Specifically, at an output speed of 984 rpm, the output torque attains its maximum value of 32.3 N·m, whereas at 912 rpm, the output torque is 31.4 N·m. Consequently, the theoretical model is capable of accurately predicting the experimental results

within the output torque range of 31.4 to 32.3 N·m.

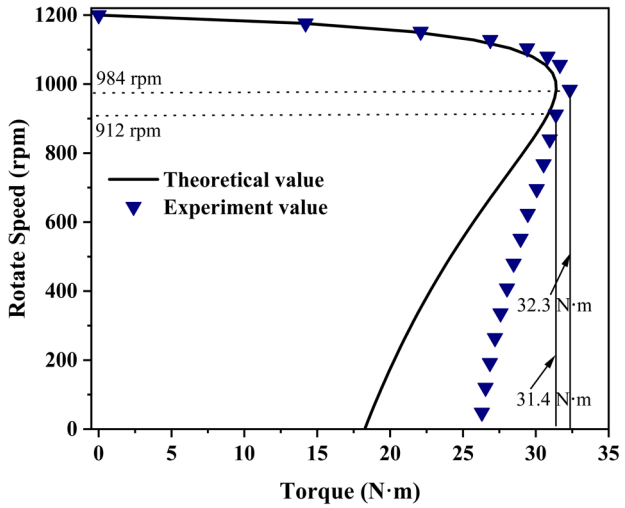

Fig. 11. Comparison of theoretical and experiment mechanical characteristic curves (g=8 mm).

Fig. 12 compares the theoretical and experimental maximum output torques of the slotted axial magnetic coupler across various air gap thicknesses. As the air gap thickness increases, a gradual decrease in the maximum output torque is observed. Notably, the errors between the theoretical and experimental maximum output torques remain consistently below 4%. Specifically, the maximum error of 3.656% occurs at an air gap thickness of 4 mm, whereas the minimum error of 2.826% is recorded at an air gap thickness of 6 mm. Consequently, this theoretical model demonstrates the capability to accurately predict the maximum output torque within the range of air gap thicknesses from 4 to 8 mm.

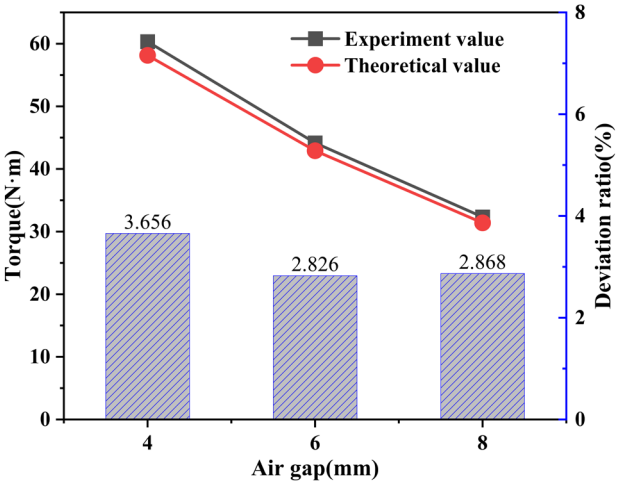

Fig. 12. Comparison of theoretical and experiment maximum output torques.

IV. Conclusion

In this paper, a new 2-D vector magnetic potential analysis model has been established to predict the output torque of the slotted axial magnetic coupler, and the experimental platform for the slotted axial magnetic coupler has been built to verify the proposed theoretical analysis model. The conclusions are as follows:

1. The output torque of the slotted axial magnetic coupler increases first and then decreases with the increase of slip ratio. When the slip ratio reaches 0.12, the output torque of the slotted axial magnetic coupler reaches its maximum value. The maximum output torque decreases with the increase of air gap thickness.

2. When the slip ratio ranges from 0 to 0.3, the theoretical torque and the experimental torque have good consistency, and the maximum deviation ratio is less than 5%. When the slip ratio exceeds 0.3, the deviation between the theoretical torque and the experimental torque gradually increases.

3. As the air gap thickness increases, the maximum output torque gradually decreases. This theoretical model can predict the maximum output torque when the air gap thickness ranges from 4 to 8 mm.

This study not only offers a user-friendly tool for conducting research analysis and engineering design pertaining to slotted axial magnetic couplers, but it also significantly contributes to the promotion of their widespread application and the advancement of supporting industries.

References

[1] Jian Wang, Heyun Lin, Shuhua Fang, and Yunkai Huang, "A General Analytical Model of Permanent Magnet Eddy Current Couplings," IEEE Transactions on Magnetics, vol. 50, no. 1, pp1–9, 2014.

[2] Xikang Cheng, Wei Liu, Yang Zhang, Sitong Liu, and Weiqi Luo, "A Concise Transmitted Torque Calculation Method for Pre-Design of Axial Permanent Magnetic Coupler," IEEE Transactions on Energy Conversion, vol. 35, no. 2, pp938–947, 2020.

[3] Wenguang Guo, Desheng Li, and Lezhi Ye, "A Model of Magnetic Field and Braking Torque in Liquid-Cooled Permanent-Magnet Retarder Accounting for the Skin Effect on Permeability," IEEE Transactions Vehicular Technology, vol. 68, no. 11, pp10618–10626, 2019.

[4] Vahid Aberoomand, Mojtaba Mirsalim, and Rasul Fesharakifard, "Design Optimization of Double-Sided Permanent-Magnet Axial Eddy-Current Couplers for Use in Dynamic Applications," IEEE Transactions on Energy Conversion, vol. 34, no. 2, pp909–920, 2019.

[5] Hamideh K. Razavi and Michanel U. Lampérth, "Eddy-current Coupling with Slotted Conductor Disk," IEEE Transactions on Magnetics, vol. 42, no. 3, pp405–410, 2006.

[6] Bojana Petkovi´c, Eva-Maria Dölker, Reinhard Schmidt, and Jens Haueisen, "Method of Fundamental Solutions Applied to 3-D Velocity Induced Eddy Current Problems," IEEE Transactions on Magnetics, vol. 54, no. 8, pp6201610, 2018.

[7] Zac Mouton and Maarten J. Kamper, "Modeling and Optimal Design of an Eddy Current Coupling for Slip-Synchronous Permanent Magnet Wind Generators," IEEE Transactions on Industrial Electronics, vol. 61, no. 7, pp3367–3376, 2014.

[8] Milad Niaz Azari and Mojtaba Mirsalim, "Line-start Permanent-magnet Motor Synchronisation Capability Improvement Using Slotted Solid Rotor," IET Electric Power Applications, vol. 7, no. 6, pp462–469, 2013.

[9] Jian Wang, Heyun Lin, Shuhua Fang, and Yunkai Huang, "A General Analytical Model of Permanent Magnet Eddy Current Couplings," IEEE Transactions on Magnetics, vol. 50, no. 1, pp8000109, 2014.

[10] Thierry Lubin and Abderrezak Rezzoug, "Steady-State and Transient Performance of Axial-Field Eddy-Current Coupling," IEEE Transactions on Industrial Electronics, vol. 62, no. 4, pp2287–2296, 2015.

[11] Xin Dai, Jiayong Cao, Yongjun Long, Qinghua Liang, Jinqiu Mo, and Shigang Wang, "Analytical Modeling of an Eddy-current Adjustable-speed Coupling System with a Three-segment Halbach Magnet Array," Electric Power Components Systems, vol. 43, no. 17, pp1891–1901, 2015.

[12] Jian Wang and Jianguo Zhu, "A Simple Method for Performance Prediction of Permanent Magnet Eddy Current Couplings Using a New Magnetic Equivalent Circuit Model," IEEE Transactions on Industrial Electronics, vol. 65, no. 3, pp2487–2495, 2018.

[13] Sajjad Mohammadi, Mojtaba Mirsalim, Sadegh Vaez-Zadeh, and Heidar Ali Talebi, “Analytical Modeling and Analysis of Axial-Flux Interior Permanent-Magnet Couplers,” IEEE Transactions on Industrial Electronics, vol. 61, no. 11, pp5940–5947, 2014.
[14] Sajjad Mohammadi, Mojtaba Mirsalim, and Sadegh Vaez-Zadeh, “Nonlinear Modeling of Eddy-current Couplers,” IEEE Transactions on Energy Conversion, vol. 29, no. 1, pp224–231, 2014.
[15] Thierry Lubin, Smail Mezani, and Abderrezak Rezzoug, “2-D Exact Analytical Model for Surface-Mounted Permanent-Magnet Motors with Semi-Closed Slots,” IEEE Transactions on Magnetics, vol. 47, no. 2, pp479–492, 2011.
[16] Thierry Lubin, Smail Mezani, and Abderrezak Rezzoug, “Development of a 2-D Analytical Model for the Electromagnetic Computation of Axial-field Magnetic Gears,” IEEE Transactions on Magnetics, vol. 49, no. 11, pp5507–5521, 2013.
[17] Frederic Dubas and Akbar Rahideh, “Two-dimensional Analytical Permanent-magnet Eddy-current Loss Calculations in Slotless PMSM Equipped with Surface-inset Magnets,” IEEE Transactions on Magnetics, vol. 50, no. 3, pp6300320, 2014.
[18] Puvan Arumugam, Tahar Hamiti, and Chris Gerada, “Estimation of Eddy Current Loss in Semi-closed Slot Vertical Conductor Permanent Magnet Synchronous Machines Considering Eddy Current Reaction Effect,” IEEE Transactions on Magnetics, vol. 49, no. 10, pp5326–5335, 2013.
[19] George Buzuzi, Mangwiro Magodora, Martin T Kudinha, William M Manamela, and Mobele H Mambo, “Steady MHD Williamson Nanofluid Flow Past an Inclined Stretching Sheet in the Presence of Heat Generation, Chemical Reaction and Aligned Magnetic Field,” IAENG International Journal of Applied Mathematics, vol. 54, no. 6, pp1125-1135, 2024.
[20] G. Shankar, and E.P. Siva, “A Numerical Investigation of Thermal and Mass Exchange of Blood Along Porous Stenosis Arterial Flow With Applied Magnetic Field,” IAENG International Journal of Applied Mathematics, vol. 54, no. 3, pp532-541, 2024.
[21] Pengwei Wang, Tianqi Gu, Binbin Sun, Rui Dang, Zhenwei Wang, Weichong Li, Tiezhu Zhang, and Yang Wang, “Control Strategy Design of Active Magnetic Levitation Bearing for High-speed Flywheel Energy Storage Device,” IAENG International Journal of Applied Mathematics, vol. 52, no. 4, pp910-917, 2022.
[22] Jinmiao Shen, Wenhui Zhang, Shuhua Zhou, and Xiaoping Ye, “Vibration Suppression Control of Space Flexible Manipulator with Varying Load Based on Adaptive Neural Network,” IAENG International Journal of Computer Science, vol. 50, no. 2, pp449-458, 2023.
[23] Qiwen Zhang, and Rongping Guo, “Prediction of Mechanical Properties of Cold Rolled Steel Using Fusion of Multi-Head Attention,” IAENG International Journal of Computer Science, vol. 51, no. 1, pp45-54, 2024.
[24] Xin Dai, Qinghua Liang, Jiayong Cao, Yongjun Long, Jinqiu Mo, and Shigang Wang, “Analytical Modeling of Axial-flux Permanent Magnet Eddy Current Couplings with a Slotted Conductor Topology,” IEEE Transactions on Magnetics, vol. 52, no. 2, pp8000315, 2016.

Ao Wang received the M.S. degree in mechanical engineering from Anhui Polytechnic University, Wuhu, Anhui, in 2023. He is currently working toward the doctorate degree with the Jiangsu University of Technology, Zhenjiang, China. His main research interests include the simulation, design, and optimization of magnetic coupling.